## **Nanoscale**



**PAPER** 

View Article Online
View Journal | View Issue



Cite this: Nanoscale, 2022, 14, 11979

# Self-assembled HfO<sub>2</sub>-Au nanocomposites with ultra-fine vertically aligned Au nanopillars†

Yizhi Zhang, <sup>©</sup> <sup>a</sup> Di Zhang, <sup>©</sup> <sup>a,b</sup> Juncheng Liu, <sup>a</sup> Ping Lu, <sup>c</sup> Julia Deitz, <sup>c</sup> Jianan Shen, <sup>a</sup> Zihao He, <sup>d</sup> Xinghang Zhang <sup>©</sup> <sup>a</sup> and Haiyan Wang <sup>©</sup> \*<sup>a,d</sup>

Oxide-metal-based hybrid materials have gained great research interest in recent years owing to their potential for multifunctionality, property coupling, and tunability. Specifically, oxide-metal hybrid materials in a vertically aligned nanocomposite (VAN) form could produce pronounced anisotropic physical properties, e.g., hyperbolic optical properties. Herein, self-assembled HfO<sub>2</sub>-Au nanocomposites with ultrafine vertically aligned Au nanopillars (as fine as 3 nm in diameter) embedded in a HfO<sub>2</sub> matrix were fabricated using a one-step self-assembly process. The film crystallinity and pillar uniformity can be obviously improved by adding an ultra-thin TiN-Au buffer layer during the growth. The HfO<sub>2</sub>-Au hybrid VAN films show an obvious plasmonic resonance at 480 nm, which is much lower than the typical plasmonic resonance wavelength of Au nanostructures, and is attributed to the well-aligned ultra-fine Au nanopillars. Coupled with the broad hyperbolic dispersion ranging from 1050 nm to 1800 nm in wavelength, and unique dielectric HfO<sub>2</sub>, this nanoscale hybrid plasmonic metamaterial presents strong potential for the design of future integrated optical and electronic switching devices.

Received 5th June 2022, Accepted 20th July 2022 DOI: 10.1039/d2nr03104c

rsc.li/nanoscale

#### 1. Introduction

Metamaterials are artificial materials that exhibit extraordinary optical, electrical, and mechanical properties that are difficult to achieve in natural materials. The metamaterials' unique properties make them valuable for applications in various fields, including chemical catalysis, for optics, and sensors. Recently significant work has been focused on enabling the multifunctionality and tunability of these metamaterials. In these metamaterials which present hyperbolic optical properties. In these metamaterials, the signs of permittivity ( $\epsilon$ ) are opposite along the in-plane (IP) and out-of-plane (OP) directions, leading to some extraordinary optical responses that have great potential in various fields such as physical research, subwavelength resolution imaging, photocatalysis, superlenses, and cloaking.

Various methods have been demonstrated for the fabrication of anisotropic metamaterials, including e-beam lithography, 17 membrane projection lithography, 18 chemical method, 19,20 electrodeposition, 21 chemical vapor deposition (CVD), 22 and physical vapor deposition (PVD). 23 Recently, pulsed laser deposition (PLD) has shown its unique advantages in fabricating complex two-phase or three-phase nanocomposite thin films, 24-26 especially for the growth of oxidemetal vertically aligned nanocomposites (VANs).7,27 VAN thin films typically consist of one phase as nanopillars embedded in the matrix phase, and show intriguing optical,28 magnetic,29 ferroelectric, and multiferroic properties,30 taking advantage of their unique vertical interface coupling. VAN hybrid structures can generate strong anisotropy compared to pure phase thin films, which makes them strong candidates for hybrid hyperbolic metamaterials. Several oxide-metal VAN systems with interesting optical properties have been successfully integrated, such as tunable localized surface plasmon resonance (LSPR) peaks in the visible and near-infrared regimes in BaTiO<sub>3</sub>-Au VANs,<sup>31</sup> hyperbolic properties for near-field electromagnetic wave manipulation in La<sub>0.67</sub>Sr<sub>0.33</sub>MnO<sub>3</sub>-Au VANs,<sup>7</sup> and highly anisotropic and hyperbolic optical responses in ZnO-Cu VAN systems.<sup>32</sup> Most of the Au nanostructures reported in VAN hybrid systems are Au nanopillars with the diameter ranging from 5 nm to 25 nm and the plasmonic resonance response ranging from 550 nm to 600 nm.33-35 The nanopillars grow epitaxially with morphology tunability

<sup>&</sup>lt;sup>a</sup>School of Materials Engineering, Purdue University, West Lafayette, 47907, USA. E-mail: hwang00@purdue.edu

<sup>&</sup>lt;sup>b</sup>Center for Integrated Nanotechnologies (CINT), Los Alamos National Laboratory, Los Alamos, NM 87545, USA

<sup>&</sup>lt;sup>c</sup>Sandia National Laboratories, Albuquerque, NM 87185, USA

<sup>&</sup>lt;sup>d</sup>School of Electrical and Computer Engineering, Purdue University, West Lafayette, 47907. USA

<sup>†</sup>Electronic supplementary information (ESI) available. See DOI: https://doi.org/ 10.1039/d2nr03104c

Paper Nanoscale

achieved by tuning the laser frequency, oxygen partial pressure, <sup>36</sup> metal composition, <sup>7</sup> and film growth thickness, <sup>2</sup> and alloying with other metals. <sup>37–39</sup>

In this work, we demonstrate the growth of self-assembled HfO<sub>2</sub>-Au VAN hybrid metamaterials fabricated using PLD. HfO<sub>2</sub> is selected as the dielectric matrix material considering its high refractive index for its broad applications as antireflection coatings, bandpass filters, beam splitters, and high reflectivity mirrors, 40-42 and its high-k dielectric nature for broad applications in the semiconductor industry. On the other hand, Au is a plasmonic material and presents broad applications in optics. Additionally, Au is a noble metal and an ideal candidate for integration with HfO2-based oxide-metal hybrid systems. A SrTiO<sub>3</sub> (a = 3.905 Å) substrate was used for nanocomposite deposition. HfO2 has multiple polymorphs including cubic, monoclinic, tetragonal and orthorhombic structures, with lattice parameters ranging from 3.26 nm to 6.39 nm, and all-dielectric materials. As shown in Fig. 1, besides the direct growth of HfO2-Au VANs, we also implemented a seed layer of TiN-Au (TiN, a = 4.249 Å) for facilitating the nucleation and growth of Au nanopillars, and to reduce the strain between thin films and the substrate. We compared the crystallinity and optical properties of the composite film with and without the seed layer for exploring the seed layer growth effects in this system.

### 2. Experimental details

#### 2.1. Thin film growth

Self-assembled thin films were deposited under vacuum using pulsed laser deposition (with a KrF excimer laser,  $\lambda=248$  nm). A buffered HfO<sub>2</sub>-Au thin film was fabricated with a two-step growth process using a TiN-Au buffer layer as a template. First, the TiN-Au layer was directly deposited on the single crystal STO (001) substrate with a TiN target. Then the HfO<sub>2</sub>-Au layer was deposited on top of the TiN-Au buffer layer with a HfN/Au target. As for the unbuffered HfO<sub>2</sub>-Au thin film, the HfO<sub>2</sub>-Au layer was directly deposited on the single crystal STO (001) substrate under the same conditions. All the films were deposited under vacuum at a temperature of 600 °C.

#### 2.2. Structural and optical characterization

The microstructure of the films was characterized by X-ray diffraction (XRD, PANalytical Empyrean), Transmission Electron Microscopy (TEM), Scanning Transmission Electron Microscopy (STEM) (an FEI TALOS 200X operated at 200 kV, and an FEI Titan™ G2 80-200 STEM with a Cs probe corrector and ChemiSTEM™ technology operated at 200 kV), and STEM electron-dispersive X-ray spectroscopy (EDS). STEM images were taken with a high-angle annular dark-field (HAADF) detector with a collection range of 60–160 mrad. The dielectric

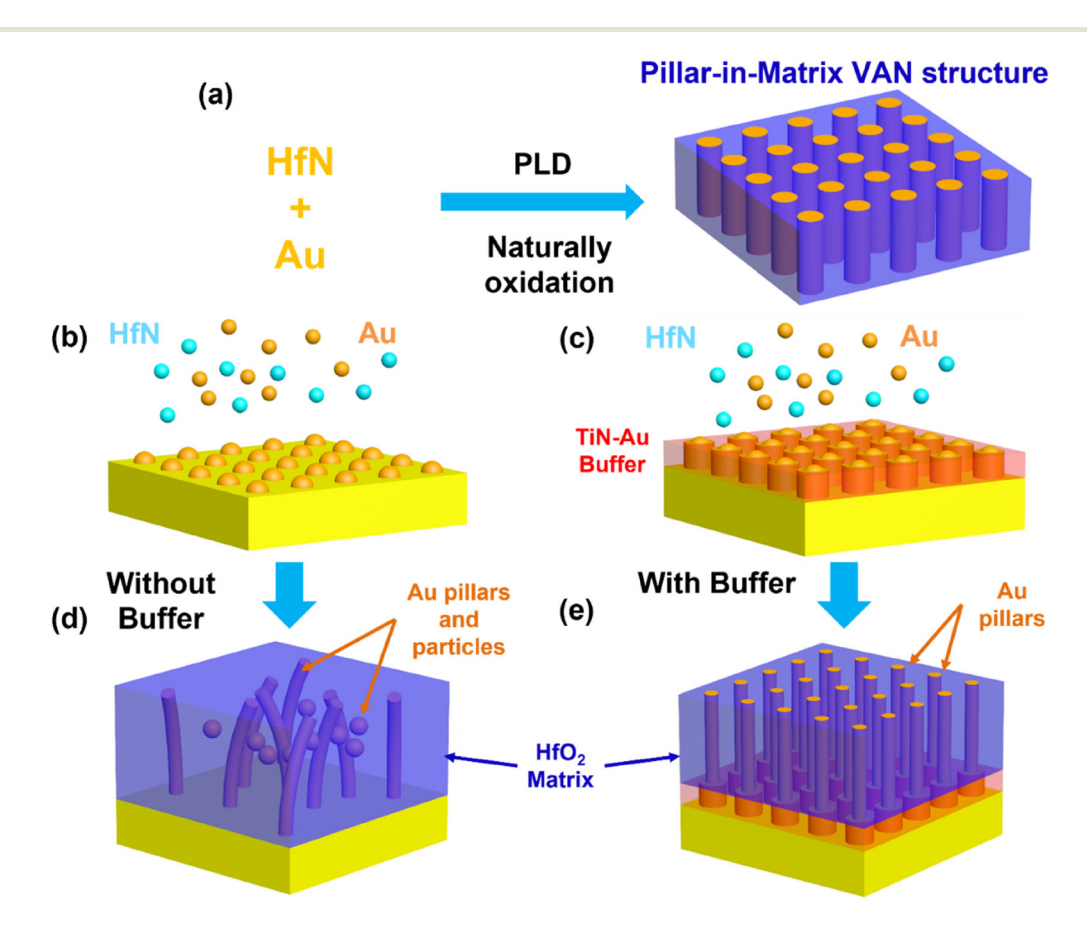


Fig. 1 Schematic of the experimental design: (a) schematic of the designed HfO<sub>2</sub>-Au VAN structure, and (b, c, d and e) schematics showing the crystallinity and orientations of the films deposited with and without TiN-Au buffer.

Nanoscale

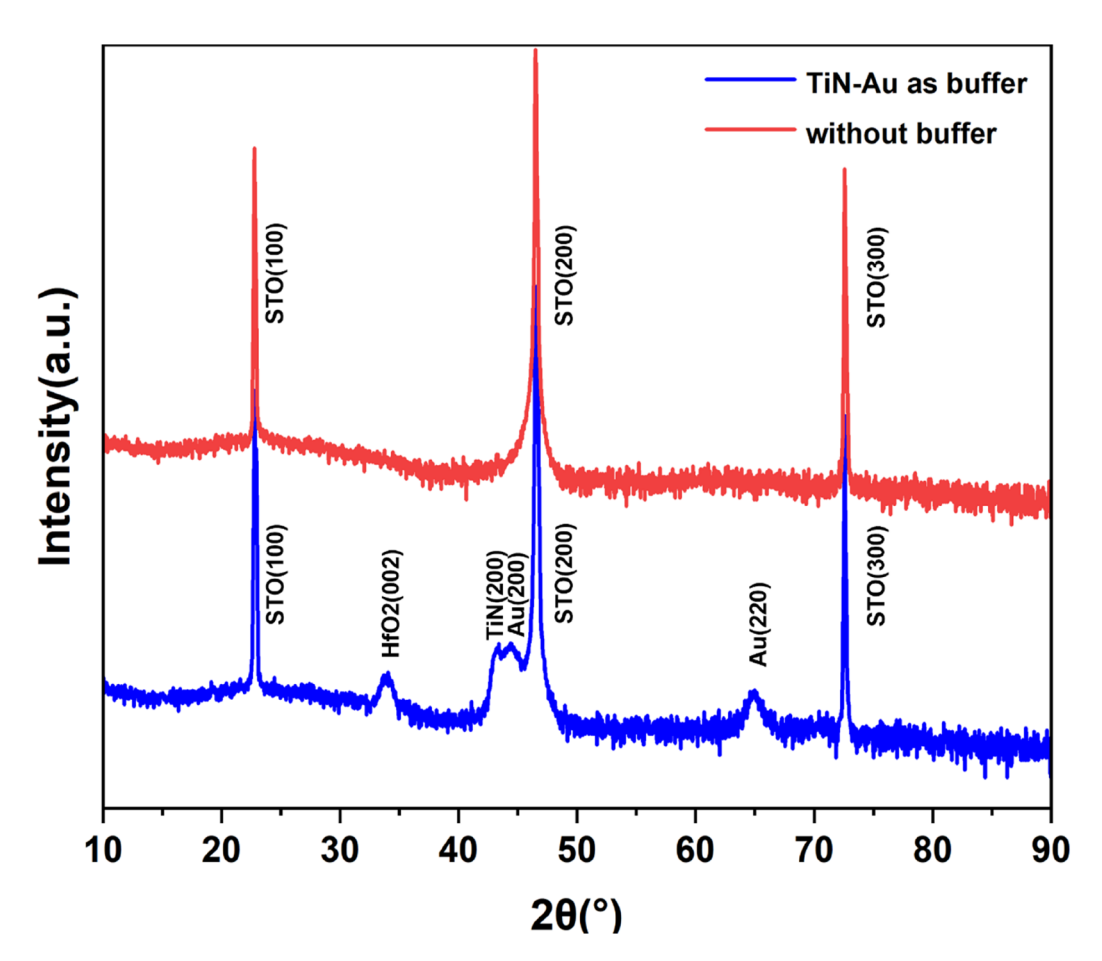


Fig. 2  $\theta$ -2 $\theta$  XRD patterns of HfO<sub>2</sub>-Au thin films grown on SrTiO<sub>3</sub> (STO) (001) with or without the TiN-Au buffer layer.

permittivity of the films was measured using a spectroscopic ellipsometer (JA Woollam RC2). The obtained data were modeled as in-plane  $(\varepsilon^{\parallel})$  and out-of-plane  $(\varepsilon^{\perp})$  components using general oscillator models to make them consistent with the Kramers-Kronig relations. The transmittance of the films was measured using a Lambda 1050 with a 3D detector (normal beam test) and a total absolute measurement system (TAMS) detector (different incident angle test).

#### 3. Results and discussion

#### Structural analysis of the HfO<sub>2</sub>-Au films by XRD

First, the crystallinity of the thin films was characterized using  $\theta$ –2 $\theta$  XRD scans. Fig. 2 shows the  $\theta$ –2 $\theta$  XRD scans of the composite films with and without the TiN-Au buffer layer. For the composite film with a TiN-Au buffer layer, a peak of 34.04° is visible, indexed as monoclinic HfO<sub>2</sub> (002), indicating the preferred (001) orientation of HfO<sub>2</sub>. According to PDF #43-1017 for HfO<sub>2</sub>, the peak at  $2\theta = 34.04^{\circ}$  corresponds to a d-spacing of 5.263 Å, which is slightly larger than the d-spacing of 5.216 Å of its bulk counterpart (or standard  $2\theta = 34.357^{\circ}$ ). This result suggests a tensile strain in the out-of-plane direction for HfO<sub>2</sub>,

which is caused by the lattice mismatch between the film and the substrate, as well as the strain between the pillars and the matrix. Clearly visible are TiN (200) at 42.86°, Au (200) at 44.42° and Au (220) at 64.97°. In comparison, only STO (100) peaks could be clearly identified from the sample without the buffer layer, indicating the poor crystal quality (i.e., much smaller grain size) and polycrystalline nature of the composite film. Since the XRD tool was set for epitaxial peak identification, the peaks from the films with poor crystal quality can be very weak. It is noted that the film diffractions can be observed in the TEM diffraction mode and will be discussed later. This poor crystal quality is likely due to the large lattice mismatch between HfO2 and STO. In short, the XRD results demonstrate that the crystallinity of the HfO2-Au thin film is improved using the TiN-Au buffer layer.

It is noted that the presence of the HfO<sub>2</sub> peak indicates the oxidation of HfN during the PLD process (as shown in Fig. S1,† the target used for deposition is a pure HfN target). To better understand the oxidation process during the deposition, a pure HfN sample was fabricated with the same HfN target under the same growth conditions. As shown in Fig. S2,† a pure HfN film can be obtained with the HfN target only, while the HfN-Au co-growth led to the formation of a

Paper Nanoscale

HfO<sub>2</sub>-Au film. It is believed that Au could assist the conversion of HfN to HfO2 during the PLD growth despite a high base vacuum of  $10^{-7}$  Torr achieved prior to the deposition.

#### 3.2 Morphology of the HfO<sub>2</sub>-Au VANs by TEM/STEM

TEM and STEM coupled with EDS analysis were performed to further characterize the microstructure of the thin films. The cross-sectional HAADF STEM image of the HfO2-Au film on STO without buffer is shown in Fig. 3a along with the schematic diagram in Fig. 3b. The total film thickness is around 60 nm. Both Au pillars and Au particles are randomly distributed inside the HfO2 matrix, with short and discontinued pillars. The selected area electron diffraction (SAED) pattern in Fig. 3f indicates that the HfO<sub>2</sub> matrix is polycrystalline with several growth orientations. In comparison, the morphology and growth quality of the HfO2-Au film were significantly improved after introducing the TiN-Au buffer layer (Fig. 3d). The VAN structure also became more ordered which is similar to the schematic drawing in Fig. 3c. Specifically, the ultra-thin Au pillars are well aligned and embedded in the HfO2 matrix and grew straight throughout the entire film. The SAED pattern, along the [100]<sub>STO</sub> zone axis shown in Fig. 3g, confirms the nearly epitaxial growth quality of HfO2 and Au with the underlying substrate as evidenced by the distinguished diffraction dots from different phases. This is consistent with the result of XRD. The EDS mapping in Fig. 3h clearly shows the distribution of Au pillars, which are uniformly embedded in both the HfO2 matrix and the TiN buffer layer.

To further understand the interfacial structure of the film, high-resolution STEM was performed on the buffered HfO<sub>2</sub>-Au film. As shown in the HAADF STEM image in Fig. 4a, the Au pillars and HfO2 matrix can be clearly distinguished with very different contrast considering the contrast is proportional to  $Z^{1.7}$ , i.e., the brighter contrast of Au vs. lower contrast in HfO<sub>2</sub>. The diameter of the pillars is around 3 nm. The local highresolution STEM image confirms that the lattice structure of the HfO<sub>2</sub> matrix is monoclinic, which agrees with the XRD results. It is worth noting that the Au pillars in HfO2 grow directly over the pillars in the TiN buffer layer, as shown in Fig. 4b. This reveals that the TiN-Au buffer layer acts as a seeding layer which improves the ordering of Au pillars.

To investigate the orientation relationship between the Au pillars and the  $HfO_2$  matrix, plan-view TEM/STEM analysis was performed. From the high-resolution STEM image shown in Fig. 4c, the out-of-plane growth orientation of Au is either [110] or [100], and the HfO<sub>2</sub> matrix is in [001], which matches the XRD results. In the HfO2 matrix, there are obvious domain structures that exist, corresponding to the 90° rotation about its [001] axis. Such a rotating domain structure could help in compensating the overall strain resulting from the asymmetric monoclinic structure. This also explains the high-quality epitaxial growth of monoclinic HfO2 around the cubic Au nanopillars. The EDS mapping and line-scan analyses shown in Fig. 4d and e further confirm the very thin diameter of the Au pillars, ~3 nm, which is smaller than previously reported Au pillars in VAN structures. 2,27,43

The laser frequency was found to play an important role in the film growth, and it can influence both pillar shape and dimension. The optimized sample shown in Fig. 3 was fabricated at a laser frequency of 2 Hz. As a comparison, a 10 Hz sample was also fabricated under the same conditions, and a cross-sectional STEM image is shown in Fig. S3.† It can be observed that some of the Au pillars can no longer grow continuously, and the pillar diameter is around 5 nm, which is much larger than that of the 2 Hz sample. This is due to the very limited diffusion time in between the pulses at 10 Hz. Therefore, a suitable frequency can be key to achieve straight, continuous, and ultra-fine Au pillars.

To investigate the difference between the directly deposited HfO<sub>2</sub> films (fabricated using the HfO<sub>2</sub> target) and the films formed by oxidation, a reference sample was fabricated with a HfO<sub>2</sub> target under the same deposition conditions as the depo-

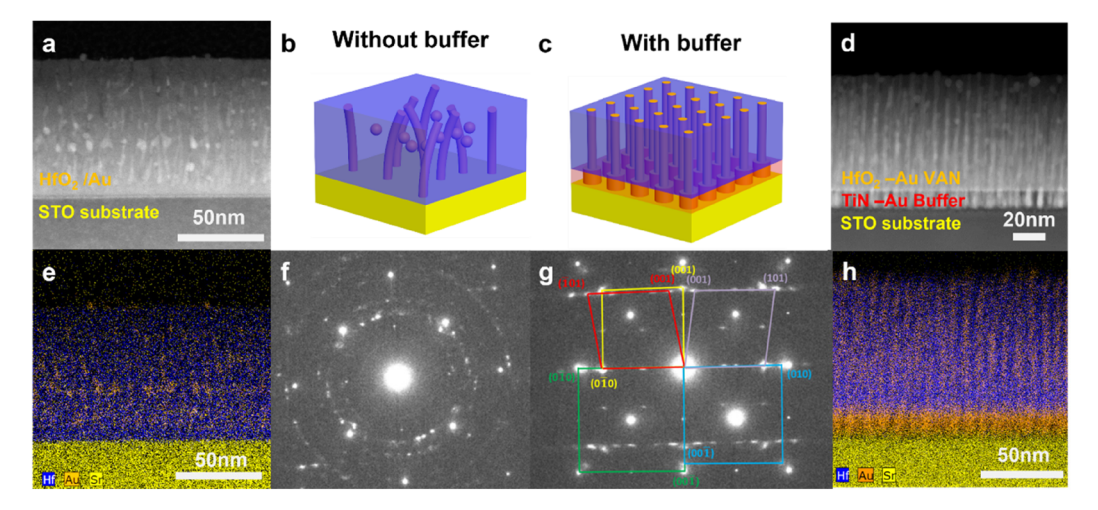


Fig. 3 Cross-sections of the HfO<sub>2</sub>-Au thin film on STO with and without TiN-Au buffer. (b and c) Schematic of the structures with and without TiN-Au buffer, (a and d) HAADF-STEM images of two films, (f and g) the corresponding diffraction patterns, and (e and h) EDS elemental maps.

Nanoscale Paper

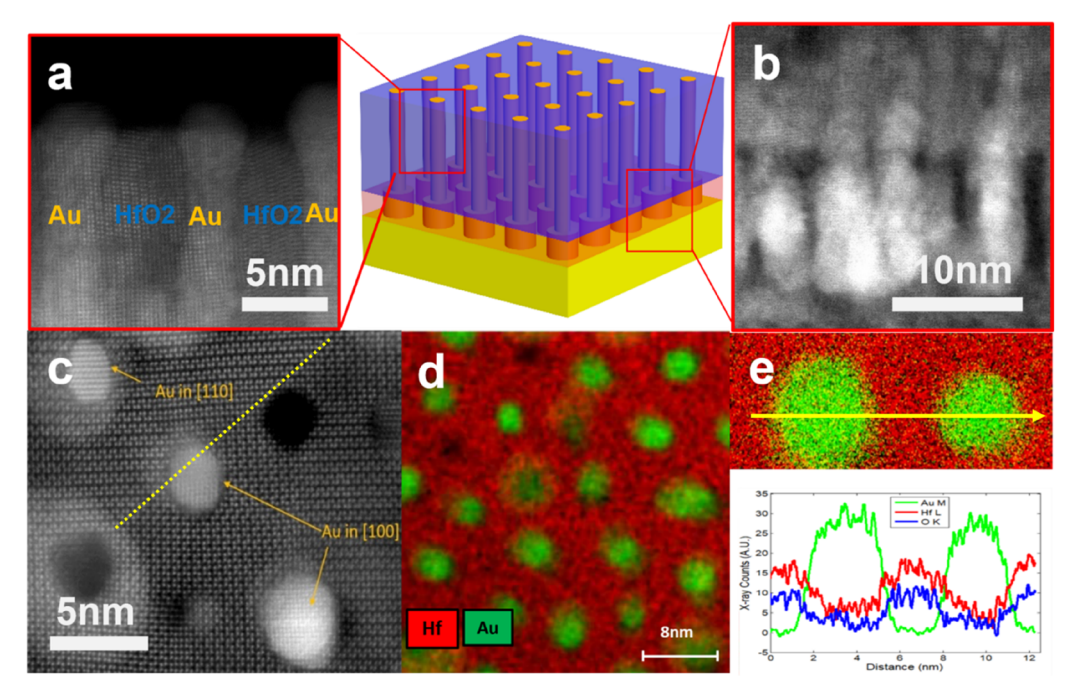


Fig. 4 STEM cross-sections and plan-view observation of the HfO<sub>2</sub>-Au thin film on STO with TiN-Au buffer. (a) Cross-sectional image at the top surface, (b) cross-sectional image at the interface between the TiN buffer layer and the HfO<sub>2</sub> film, (c) plan-view image of the film tilted to the HfO<sub>2</sub> [001] projection, (d) EDS elemental maps of the film in the plane view (Hf-red, Au-green), and (e) EDS elemental maps along with the EDS line profiles across two Au columns. The yellow dashed-line in (c) indicates a domain boundary position.

sition using the HfN target. As shown in Fig. S4(a) and (b),† Au pillars in the directly deposited HfO2 film were obviously tilted. This is likely due to the monoclinic structure of the HfO2 matrix. HfN, in contrast, has a cubic structure, and therefore, the Au pillars can grow straight in the initial stage of the film growth using the HfN target, and the further oxidation process converts HfN to HfO2 during the remaining deposition. The high-resolution TEM image shown in Fig. S4(c)† reveals that the Au pillars grow inside the monoclinic HfO2 matrix by interface steps, leading to tilted Au pillars.

To better understand the oxidation process, a comparison sample was fabricated at room temperature. STEM images and EDS elemental mapping of this RT sample are shown in Fig. S6.† It can be observed that Au grows as nanoparticles embedded in the HfN matrix at room temperature. Based on the EDS elemental mapping, only the very top surface portion (5 nm) of the HfN film was oxidized, and a clear contrast edge can be distinguished at the top of the HfN film in the HAADF image. This suggests that oxidation likely occurred during the cooling process after the deposition.

Since Au is embedded in the HfN matrix in the HfN-Au film, there are a lot of phase boundaries between Au and HfN, and these vertical phase boundaries can act as an oxygen diffusion path. Previous research reveals that oxygen can diffuse faster through the grain boundaries and phase boundaries. 44,45 In the pure HfN film, the amount of grain/ phase boundaries is much less than that in the HfN-Au film. Therefore, the existence of Au nanopillars and vertical phase boundaries could assist the oxidation process of the HfN film.

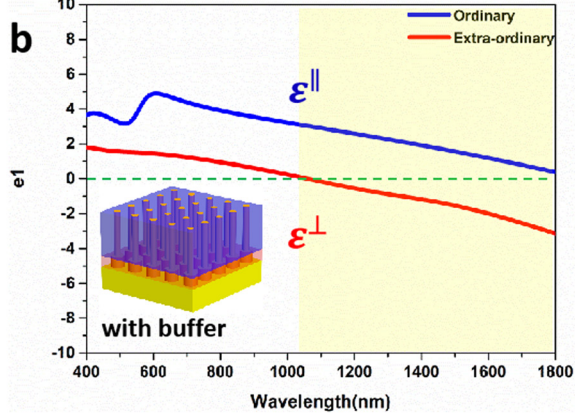
#### 3.3 Optical properties of the HfO<sub>2</sub>-Au VANs

To investigate the optical properties of the HfO<sub>2</sub>-Au films, ellipsometry measurement was performed. The dielectric constants were calculated and are presented in Fig. 5a and b. Due to the anisotropic structure of the film, the obtained data were modeled as in-plane  $(\varepsilon^{\parallel})$  and out-of-plane  $(\varepsilon^{\perp})$  components using general oscillator models to make them consistent with Kramers-Kronig relations. A hyperbolic region between 1050 nm and 1800 nm could be observed in the buffered HfO<sub>2</sub>-Au thin film, where the out-of-plane permittivity is negative while the in-plane permittivity is positive. The film without a buffer layer shows no obvious hyperbolic region, which could be due to the random distribution of the Au pillars and particles inside the film. The anisotropic optical properties make this buffered HfO<sub>2</sub>-Au film an ideal hyperbolic metamaterial for different optical applications.<sup>15</sup>

In addition, transmittance measurement was also performed on both thin films. As shown in Fig. 5c, clear absorption valleys could be observed for both thin films. In the buffered HfO<sub>2</sub>-Au thin film, only a strong adsorption peak can be distinguished at 480 nm, which results from the plasmon resonance of Au pillars. Simulated electric field maps under a 480 nm incident beam by COMSOL simulation are shown in Fig. S8,† which agree well with the plasmonic resonance of Au pillars. The plasmonic resonance wavelength is much smaller than previously reported data, which is from 550 nm to 600 nm (marked as a yellow region in Fig. 5c). 33-35 This could be due to the low diameter of ultra-thin Au pillars, since the

Paper

Ordinary Extra-ordinar a  $\boldsymbol{arepsilon}^{\parallel}$ 2 e1  $oldsymbol{arepsilon}^\perp$ -2 -R without buffer -10 600 800 400 1000 1200 1400 1600 1800 Wavelength(nm) 10 Ordinary b 8 Extra-ordinar 6



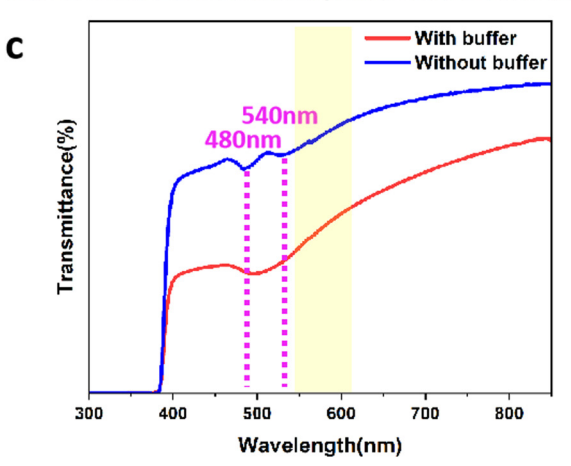


Fig. 5 Optical properties. Dielectric constant e1 of the HfO<sub>2</sub>-Au film (a) without buffer and (b) with buffer. (c) The transmittance of HfO<sub>2</sub>-Au on STO (001) with and without TiN-Au buffer.

plasmonic absorption peak can have a redshift as the size increases.<sup>33</sup> The unbuffered HfO<sub>2</sub>-Au thin film shows two plasmonic peaks at 480 nm and 540 nm, which could result from Au pillars and Au particles, respectively. The plasmonic properties could be used in the design of future sensor devices.

To explore the changes in transmittance as a function of the incident angle, we have performed an angular dependent transmittance test on the buffered sample using a Lambda UVvis system with a TAMS detector, since the Au nanowires could exhibit two plasmon resonances with different electrical field directions. As shown in Fig. S7,† the plasmon resonance peak is still around 490 nm, but more contribution from a higher wavelength region can be observed which may result from the different dimensions of Au pillars viewed from different angles. It is also noted that the plasmon resonance can be influenced by several factors, such as matrix materials and interactions between Au pillars. Therefore, the results of the Au pillars in HfO<sub>2</sub> could be different from the results of individual Au nanowires.

Overall, this study presents a new approach for preparing HfO<sub>2</sub> based VAN thin films with very fine and highly aligned thin Au nanopillars. By adding a suitable buffer layer, the crystallinity of the films and the nanopillar ordering were obviously improved, which indicates the importance of the strain effect during PLD growth. The as-deposited HfO2-Au thin film shows strong anisotropic optical properties, which make it ideal as a hybrid metamaterial. However, the oxidation mechanism of HfN under HfN-Au deposition is still under investigation. HfN, deposited by itself, results in pure HfN films while the HfN-Au composite target deposition will result in HfO<sub>2</sub>-Au films. The incorporation of Au is believed to facilitate the overall oxidation process of HfN during growth. Further research is undergoing to explore the fundamental mechanisms for the HfN oxidation process facilitated by the presence of Au. It is interesting to note that the TiN-Au and TaN-Au VAN systems under the same growth conditions did not result in obvious oxidation issues during the composite growth, in comparison. 26,28,48,49 Further work could focus on tuning the growth parameters for limiting the oxidation process of HfN. For example, the higher deposition rate and high flux of the adatoms could limit the diffusion and oxidation processes as the primary nitride oxidation mechanisms have been reported based on diffusion and surface reactions. 50,51 On the other hand, HfO2 is also a good candidate for memristor devices, and such HfO2-Au VANs are coupled in memristor designs for achieving novel filamentary switching properties. This unique nanocomposite system could also find applications in optics, such as hyperbolic properties in quantum nanophotonic applications, 52 gainassisted hyperlenses and tunable nonlinear imaging devices, as well as in plasmonic properties in the design of sensing devices.15

#### 4. Conclusion

In summary, self-assembled HfO<sub>2</sub>-Au nanocomposite thin films with ultra-thin Au nanopillars of 3 nm have been successfully deposited on STO substrates using an HfN target through a direct conversion process during deposition. During the PLD process, HfN was naturally oxidized to HfO<sub>2</sub> during the co-growth of HfN-Au. The crystallinity of the film and the ordering of the Au nanopillars are improved by adding a TiN-Au buffer layer. The plasmonic resonance of the HfO<sub>2</sub>-Au VANs grown on TiN-Au buffer occurs at a wavelength of around

480 nm due to the ultra-fine Au pillars. The hyperbolic transition region of the TiN-Au buffered film ranges from 1050 nm to 1800 nm. This work paves a new way to fabricate  $HfO_2$ -metal hybrid nanocomposites with strong anisotropic structures and optical properties for future optics and electronics.

#### Conflicts of interest

Nanoscale

The authors have no conflicts of interest to declare.

## Acknowledgements

This work was supported by the U.S. National Science Foundation DMR-2016453 and DMR-1565822 (VAN thin film growth and High-resolution STEM work). This work was performed, in part, at the Center for Integrated Nanotechnologies, an Office of Science User Facility operated for the U.S. Department of Energy (DOE) Office of Science. Los Alamos National Laboratory, an affirmative action equal opportunity employer, is managed by Triad National Security, LLC for the U.S. Department of Energy's NNSA, under contract 89233218CNA000001. The microscopy work was partially supported by the Laboratory Directed Research and Development program at Sandia National Laboratories. Sandia National Laboratories is a multi-mission laboratory managed and operated by National Technology and Engineering Solutions of Sandia, LLC., a wholly owned subsidiary of Honeywell International, Inc., for the U.S. Department of Energy's National Nuclear Security Administration under Contract No. DE-NA0003525. This paper describes the objectives of technical results and analysis. Any subjective views or opinions that might be expressed in the paper do not necessarily represent the views of the U.S. Department of Energy or the United States Government.

#### References

- 1 D. Zhang and H. Wang, Self-Assembled Metal-Dielectric Hybrid Metamaterials in Vertically Aligned Nanocomposite Form with Tailorable Optical Properties and Coupled Multifunctionalities, *Adv. Photonics Res.*, 2021, 2(5), 2000174.
- 2 D. Zhang, S. Misra, L. Li, X. Wang, J. Jian, P. Lu, et al., Tunable Optical Properties in Self-Assembled Oxide-Metal Hybrid Thin Films via Au-Phase Geometry Control: From Nanopillars to Nanodisks, Adv. Opt. Mater., 2020, 8(4), 1901359.
- 3 D. Zhang, P. Lu, S. Misra, A. Wissel, Z. He, Z. Qi, et al., Design of 3D Oxide–Metal Hybrid Metamaterial for Tailorable Light–Matter Interactions in Visible and Near–Infrared Region, Adv. Opt. Mater., 2021, 9(1), 2001154.

- 4 W. Cai, U. K. Chettiar, A. V. Kildishev and V.M. Shalaev, Optical cloaking with metamaterials, *Nat. Photonics*, 2007, 1(4), 224–227.
- 5 C. Ray and T. Pal, Retracted Article: Recent advances of metal-metal oxide nanocomposites and their tailored nanostructures in numerous catalytic applications, *J. Mater. Chem. A*, 2017, 5(20), 9465–9487.
- 6 M. Cargnello, M. Grzelczak, B. Rodríguez-González, Z. Syrgiannis, K. Bakhmutsky, V. La Parola, et al., Multiwalled carbon nanotubes drive the activity of metal@ oxide core-shell catalysts in modular nanocomposites, J. Am. Chem. Soc., 2012, 134(28), 11760–11766.
- 7 J. Huang, H. Wang, Z. Qi, P. Lu, D. Zhang, B. Zhang, et al., Multifunctional Metal–Oxide Nanocomposite Thin Film with Plasmonic Au Nanopillars Embedded in Magnetic La0. 67Sr0. 33MnO3 Matrix, Nano Lett., 2021, 21(2), 1032– 1039.
- 8 P. Rai, S. M. Majhi, Y.-T. Yu and J.-H. Lee, Noble metal@metal oxide semiconductor core@shell nano-architectures as a new platform for gas sensor applications, *RSC Adv.*, 2015, 5(93), 76229–76248.
- 9 N. I. Zheludev and Y. S. Kivshar, From metamaterials to metadevices, *Nat. Mater.*, 2012, 11(11), 917–924.
- 10 O. Hess, J. B. Pendry, S. A. Maier, R. F. Oulton, J. M. Hamm and K. L. Tsakmakidis, Active nanoplasmonic metamaterials, *Nat. Mater.*, 2012, 11(7), 573–584.
- 11 D. Smith and D. Schurig, Electromagnetic wave propagation in media with indefinite permittivity and permeability tensors, *Phys. Rev. Lett.*, 2003, **90**(7), 077405.
- 12 J. Li, L. Fok, X. Yin, G. Bartal and X. Zhang, Experimental demonstration of an acoustic magnifying hyperlens, *Nat. Mater.*, 2009, **8**(12), 931–934.
- 13 J. Yao, Z. Liu, Y. Liu, Y. Wang, C. Sun, G. Bartal, *et al.*, Optical negative refraction in bulk metamaterials of nanowires, *Science*, 2008, 321(5891), 930–930.
- 14 A. A. High, R. C. Devlin, A. Dibos, M. Polking, D. S. Wild, J. Perczel, *et al.*, Visible-frequency hyperbolic metasurface, *Nature*, 2015, 522(7555), 192–196.
- 15 A. Poddubny, I. Iorsh, P. Belov and Y. Kivshar, Hyperbolic metamaterials, *Nat. Photonics*, 2013, 7(12), 948–957.
- 16 J. J. Mock, D. R. Smith and S. Schultz, Local refractive index dependence of plasmon resonance spectra from individual nanoparticles, *Nano Lett.*, 2003, 3(4), 485– 491.
- 17 N. Liu, H. Guo, L. Fu, S. Kaiser, H. Schweizer and H. Giessen, Three-dimensional photonic metamaterials at optical frequencies, *Nat. Mater.*, 2008, 7(1), 31–37.
- 18 D. B. Burckel, J. R. Wendt, G. A. Ten Eyck, J. C. Ginn, A. R. Ellis, I. Brener, *et al.*, Micrometer–scale cubic unit cell 3D metamaterial layers, *Adv. Mater.*, 2010, 22(44), 5053–5057.
- 19 M. Murdoch, G. Waterhouse, M. Nadeem, J. Metson, M. Keane, R. Howe, *et al.*, The effect of gold loading and particle size on photocatalytic hydrogen production from

**Paper** 

- ethanol over Au/TiO2 nanoparticles, Nat. Chem., 2011, 3(6), 489-492.
- 20 T. C. Damato, C. C. de Oliveira, R. A. Ando and P. H. Camargo, A facile approach to TiO2 colloidal spheres decorated with Au nanoparticles displaying well-defined sizes and uniform dispersion, Langmuir, 2013, 29(5), 1642-1649.
- 21 K. L. Zhou, Z. Wang, C. B. Han, X. Ke, C. Wang, Y. Jin, et al., Platinum single-atom catalyst coupled with transition metal/metal oxide heterostructure for accelerating alkaline hydrogen evolution reaction, Nat. Commun., 2021, 12(1), 1-10.
- 22 D. Barreca, G. Carraro, E. Comini, A. Gasparotto, C. Maccato, C. Sada, et al., Novel synthesis and gas sensing performances of CuO-TiO2 nanocomposites functionalized with Au nanoparticles, J. Phys. Chem. C, 2011, 115(21), 10510-10517.
- 23 A. Honciuc, M. Laurin, S. Albu, M. Sobota, P. Schmuki and I. Libuda, Controlling the adsorption kinetics via nanostructuring: Pd nanoparticles on TiO2 nanotubes, Langmuir, 2010, 26(17), 14014-14023.
- 24 J. Huang, D. Zhang, J. Liu and H. Wang, Freestanding La0. 7Sr0. 3MnO3: NiO vertically aligned nanocomposite thin films for flexible perpendicular interfacial exchange coupling, Mater. Res. Lett., 2022, 10(4), 287-294.
- 25 X. Wang, J. Jian, H. Wang, J. Liu, Y. Pachaury, P. Lu, et al., Nitride-Oxide-Metal Heterostructure with Self-Assembled Core-Shell Nanopillar Arrays: Effect of Ordering on Magneto-Optical Properties, Small, 2021, **17**(5), 2007222.
- 26 X. Wang, J. Jian, S. Diaz-Amaya, C. E. Kumah, P. Lu, J. Huang, et al., Hybrid plasmonic Au-TiN vertically aligned nanocomposites: a nanoscale platform towards tunable optical sensing, Nanoscale Adv., 2019, 1(3), 1045-1054.
- 27 J. Liu, X. Wang, X. Gao, H. Wang, J. Jian, J. Huang, et al., Multifunctional self-assembled BaTiO3-Au nanocomposite thin films on flexible mica substrates with tunable optical properties, Appl. Mater. Today, 2020, 21, 100856.
- 28 J. Huang, X. Wang, D. Li, T. Jin, P. Lu, D. Zhang, et al., 3D hybrid plasmonic framework with Au nanopillars embedded in nitride multilayers integrated on Si, Adv. Mater. Interfaces, 2020, 7(17), 2000493.
- 29 A. Chen, Z. Bi, H. Hazariwala, X. Zhang, Q. Su, L. Chen, et al., Microstructure, magnetic, and low-field magnetotransport properties of self-assembled (La0. 7Sr0. 3MnO3) 0.5:(CeO<sub>2</sub>) 0.5 vertically aligned nanocomposite thin films, Nanotechnology, 2011, 22(31), 315712.
- 30 O. J. Lee, S. Misra, H. Wang and J. MacManus-Driscoll, Ferroelectric/multiferroic self-assembled vertically aligned nanocomposites: Current and future status, APL Mater., 2021, 9(3), 030904.
- 31 M. Kalaswad, D. Zhang, X. Gao, L. L. Contreras, H. Wang, X. Wang, et al., Integration of Hybrid Plasmonic Au-BaTiO3 Metamaterial on Silicon Substrates, ACS Appl. Mater. Interfaces, 2019, 11(48), 45199-45206.

- 32 J. Huang, X. Wang, X. L. Phuah, P. Lu, Z. Qi and H. Wang, Plasmonic Cu nanostructures in ZnO as hyperbolic metamaterial thin films, Mater. Today Nano, 2019, 8, 100052.
- 33 J. Huang, T. Jin, S. Misra, H. Wang, Z. Qi, Y. Dai, et al., Tailorable optical response of Au-LiNbO3 hybrid metamaterial thin films for optical waveguide applications, Adv. Opt. Mater., 2018, 6(19), 1800510.
- 34 S. Misra, L. Li, D. Zhang, J. Jian, Z. Qi, M. Fan, et al., Self-Assembled Ordered Three-Phase Au-BaTiO3-ZnO Vertically Aligned Nanocomposites Achieved Templating Method, Adv. Mater., 2019, 31(7), 1806529.
- 35 D. Zhang, Z. Qi, J. Jian, J. Huang, X. L. Phuah, X. Zhang, et al., Thermally Stable Au-BaTiO3 Nanoscale Hybrid High-Temperature Metamaterial for Plasmonic Applications, ACS Appl. Nano Mater., 2020, 3(2), 1431-1437.
- 36 R. L. Paldi, X. Sun, X. L. Phuah, J. Lu, X. Zhang, A. Siddiqui, et al., Deposition pressure-induced microstructure control and plasmonic property tuning in hybrid ZnO-Ag x Au 1- x thin films, Nanoscale Adv., 2021, 3(10), 2870-2878.
- 37 D. Zhang, S. Misra, J. Jian, P. Lu, L. Li, A. Wissel, et al., Self-Assembled BaTiO3-Au x Ag1-x Low-Loss Hybrid Plasmonic Metamaterials with an Ordered "Nano-Dominolike" Microstructure, ACS Appl. Mater. Interfaces, 2021, 13(4), 5390-5398.
- 38 R. L. Paldi, J. Lu, Y. Pachaury, Z. He, N. A. Bhatt, X. Zhang, et al., ZnO-Au x Cu1- x Alloy and ZnO-Au x Al1- x Alloy Vertically Aligned Nanocomposites for Low-Loss Plasmonic Metamaterials, Molecules, 2022, 27(6), 1785.
- J. Huang, X. L. Phuah, L. M. McClintock, P. Padmanabhan, K. Vikrant, H. Wang, et al., Core-shell metallic alloy nanopillars-in-dielectric hybrid metamaterials magneto-plasmonic coupling, Mater. Today, 2021, 51, 39-47.
- 40 J. M. Khoshman and M. E. Kordesch, Optical properties of a-HfO2 thin films, Surf. Coat. Technol., 2006, 201(6), 3530-
- 41 T. Tan, Z. Liu, H. Lu, W. Liu and H. Tian, Structure and optical properties of HfO2 thin films on silicon after rapid thermal annealing, Opt. Mater., 2010, 32(3), 432-435.
- 42 M. Fadel, M. O. Azim, O. Omer and R. Basily, A study of some optical properties of hafnium dioxide (HfO2) thin films and their applications, Appl. Phys. A, 1998, 66(3), 335-343.
- 43 L. Li, L. Sun, J. S. Gomez-Diaz, N. L. Hogan, P. Lu, F. Khatkhatay, et al., Self-assembled epitaxial Au-Oxide vertically aligned nanocomposites for nanoscale metamaterials, Nano Lett., 2016, 16(6), 3936-3943.
- 44 R. Hoffman and D. Turnbull, Lattice and grain boundary self-diffusion in silver, J. Appl. Phys., 1951, 22(5), 634-639.
- 45 R. A. De Souza, M. J. Pietrowski, U. Anselmi-Tamburini, S. Kim, Z. A. Munir and M. Martin, Oxygen diffusion in nanocrystalline yttria-stabilized zirconia: the effect of grain

boundaries, Phys. Chem. Chem. Phys., 2008, 10(15), 2067-

Nanoscale

- 2072.
- 46 Q. Xu, J. Bao, F. Capasso and G. M. Whitesides, Surface plasmon resonances of free-standing gold nanowires fabricated by nanoskiving, *Angew. Chem., Int. Ed.*, 2006, 45(22), 3631–3635.
- 47 V. Amendola, R. Pilot, M. Frasconi, O. M. Maragò and M. A. Iatì, Surface plasmon resonance in gold nanoparticles: a review, *J. Phys.: Condens. Matter*, 2017, **29**(20), 203002.
- 48 X. Wang, J. Choi, J. Liu, O. Malis, X. Li, P. Bermel, *et al.*, 3D Hybrid Trilayer Heterostructure: Tunable Au Nanorods and Optical Properties, *ACS Appl. Mater. Interfaces*, 2020, **12**(40), 45015–45022.
- 49 J. Huang, X. Wang, N. L. Hogan, S. Wu, P. Lu, Z. Fan, *et al.*, Nanoscale artificial plasmonic lattice in self–assembled vertically aligned nitride–metal hybrid metamaterials, *Adv. Sci.*, 2018, 5(7), 1800416.
- 50 A. Zakutayev and C. L. Perkins, Influence of protection layers on thermal stability of nitride thin films, *Phys. Status Solidi RRL*, 2021, **15**(8), 2100178.
- 51 R. W. Harrison and W. E. Lee, Mechanism and kinetics of oxidation of ZrN ceramics, *J. Am. Ceram. Soc.*, 2015, **98**(7), 2205–2213.
- 52 C. Cortes, W. Newman, S. Molesky and Z. Jacob, Quantum nanophotonics using hyperbolic metamaterials, *J. Opt.*, 2012, **14**(6), 063001.